LANGMUIR

pubs.acs.org/Langmuir Article

Molecular Dynamics Simulations of Water Condensation on Surfaces with Tunable Wettability

Dineli T. S. Ranathunga, Alexandra Shamir, Xianming Dai, and Steven O. Nielsen*

Cite This: *Langmuir* 2020, 36, 7383–7391 Read Online

ACCESS | Metrics & More | Article Recommendations | Supporting Information

ABSTRACT: Water condensation plays a major role in a wide range of industrial applications. Over the past few years, many studies have shown interest in designing surfaces with enhanced water condensation and removal properties. It is well known that heterogeneous nucleation outperforms homogeneous nucleation in the condensation process. Because heterogeneous nucleation initiates on a surface at a small scale, it is highly desirable to characterize water-surface interactions at the molecular level. Molecular dynamics (MD) simulations can provide direct insight into heterogeneous nucleation and advance surface designs. Existing MD simulations of water condensation on surfaces were conducted by tuning the solid-water van der Waals interaction energy as a substitute for modeling surfaces with different wettabilities. However, this approach cannot reflect the real intermolecular interactions between the surface and water molecules. Here, we report MD simulations of water condensation on realistic surfaces of alkanethiol self-assembled monolayers with different head group chemistries. We show that decreasing surface hydrophobicity significantly increases the electrostatic forces between water molecules and the surface, thus increasing the water condensation rate. We observe a strong correlation between our rate of condensation results and the results from other surface characterization metrics, such as the interfacial thermal conductance, contact angle, and the molecular-scale wettability metric of Garde and co-workers. This work provides insight into the water condensation process at the molecular scale on surfaces with tunable wettability.

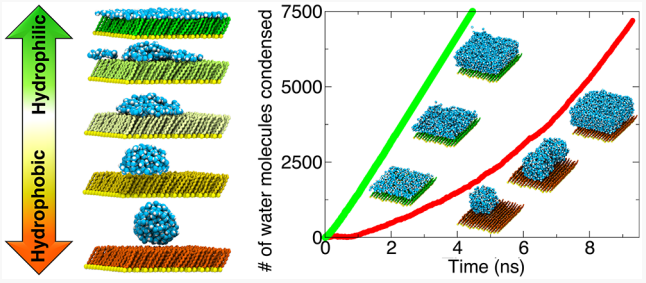

INTRODUCTION

The condensation of water vapor on a cooled surface is significant for water harvesting,[1−4] desalination,[5,6] thermal management,[7−9] and power generation.[10] Water capture by vapor condensation on a surface can occur in a dropwise or film-wise manner. One would expect dropwise condensation on a hydrophobic surface and film-wise condensation on a hydrophilic surface. Hydrophilic surfaces have a lower nucleation barrier, but the resulting film-wise condensate is not desired because of its slow removal rate. Thus, hydrophilic surfaces are good at capturing water but have poor removal capabilities. Conversely, hydrophobic surfaces are poor at capturing water but have excellent removal characteristics. This tension between rapid water capture and removal has led to sophisticated surface designs to obtain both characteristics. For example, over the past few years, many studies have shown interest in designing superhydrophobic surfaces (SHS),[11−13] patterned SHS,[14−16] or liquid-infused surfaces[17,18] to enhance either condensation nucleation or droplet removal. Recently, a hydrophilic directional slippery rough surface (SRS) was designed for water harvesting using salient features of pitcher plants and rice leaves. The SRS surface has nanotextures infused with hydrophilic lubricant on directional microgrooves for enhanced droplet nucleation and removal.[1] To improve the design of these surfaces, a molecular-scale understanding of the water-surface interactions as a function of surface wettability is desired.

Significant effort has gone into quantifying the role of surface wettability on water condensation.[19−30] For example, Xu et al.[19] studied the nucleation process on an atomically flat solid surface with a tunable solid-water interaction energy using molecular dynamics (MD) computer simulations. They have considered only dispersion interactions between surface atoms and water. Interestingly, they observed that at low interaction energy, small water clusters on the surface tend to escape into the vapor phase, which can subsequently serve as homogeneous nucleation sites. At higher energy, they observed mainly heterogeneous nucleation with concomitant suppression of clusters in the vapor phase.

In practical applications, surfaces typically feature hydrophobic or hydrophilic functional groups. The interaction between a hydrophilic functional group and a water molecule is

Received: March 31, 2020
Revised: June 5, 2020
Published: June 5, 2020

https://dx.doi.org/10.1021/acs.langmuir.0c00915
Langmuir 2020, 36, 7383–7391

dominated by electrostatics, whose energy scales as the inverse distance, whereas dispersion energies scale as the sixth power of inverse distance. Therefore, approaches in which hydrophilicity is substituted for a van der Waals interaction are fundamentally flawed. We used self-assembled monolayer (SAM) surfaces of alkanethiols with different head group chemistries for the condensation studies. Because we use a fully atomistic force field, the surfaces interact with water molecules through both dispersion and electrostatic forces. In our approach, we can incorporate electron-withdrawing atoms such as nitrogen and oxygen into the SAM head group to tune the surface from completely hydrophobic ($-CH_3$) to completely hydrophilic ($-OH$). Another advantage of these surfaces is that they are extremely well characterized both experimentally and computationally.

We quantify the role of surface wettability on water vapor condensation and correlate our results with the role of surface wettability on interfacial thermal conductance and in the compressibility of liquid water in the vicinity of the surface. The effect of surface wettability on heat transfer is well characterized and depends on, among other factors, the contact angle (which affects the surface area of contact) and the Kapitza resistance.[31,32] For SAMs, Shenogina et al.[31] studied how wetting affects the heat transfer and showed that the Kapitza interfacial thermal conductance is proportional to $(1 + \cos\theta)$ via MD simulations, where θ is the water droplet contact angle in air. Garde and co-workers proposed the use of solvent density fluctuations as a signature of the wettability of a surface, characterized by the compressibility of interfacial water. Specifically, they observed that water density fluctuations are enhanced near hydrophobic surfaces, whereas hydrophilic surfaces quench the fluctuations because of hydrogen bond formation.[33] The comparison of these disparate metrics gives us a more complete picture of the role of surface wettability in the behavior of water.

In this study, we focused on heterogeneous nucleation but not on droplet removal. The rate of condensation was studied using two different models: 1. with a fixed amount of water (initially all in the vapor phase) and 2. with a constant vapor density. A condensation study using a constant vapor density has been done previously for Lennard–Jones particles[24] but not for water. We provide molecular insight into the condensation mechanism as a function of surface chemistry. From density and hydrogen bond analysis, we study the structural behavior of water at the interface and quantify the water penetration into the SAM layer, the arrangement of water molecules near the SAM, and the stability of water clusters on the surface. To further quantify the water interactions with the surface, we calculate the interaction energy between water and the SAM. In our study, we explore the molecular-level details of water condensation on surfaces of different wettabilities and provide connections with macroscopic surface characterizations. Our results provide important guidance toward surface design to promote heterogeneous nucleation in condensation heat transfer.

METHODOLOGY AND SIMULATION DETAILS

Models. To characterize surface wettability, eight different homogeneous SAMs were created. All SAMs were made with 10 carbon long alkanethiol molecules (Figure S1). One end of each alkanethiol molecule was terminated with a sulfur atom fixed in place to mimic chemisorption to a gold (111) surface. The other end was terminated with different hydrophilic and hydrophobic functional groups, specifically $-CH_3$, $-OCH_3$, $-CONH_2$, $-CONHCH_3$, $-COOH$, $-CN$, $-OH$, and $-CF_3$ to make homogeneous SAM surfaces. For the $-CF_3$-terminated SAM, the carbon backbone is fully fluorinated ($S(CF_2)_{10}-CF_3$). Hence, throughout this paper, the label $-CF_3$ is used to define the fully fluorinated (perfluorodecanethiol) SAM.

All SAM systems, except the fully fluorinated one, consist of 224 alkanethiols ($S(CH_2)_{10}$-R) in a 70 × 69.2 × 305 Å^3 simulation box with the surface normal in the z-direction. The experimentally known area per alkanethiol molecule of 21.6 Å^2 was used with lattice constant $a = 5\sqrt{2}$ and tilt angle 30° for the initial condition.[34] The fully fluorinated system used a 82.6 × 81.8 × 305 Å^3 simulation box with 30.1 Å^2 area per thiol molecule and lattice constant $a = 5.9\sqrt{2}$.[35]

All eight SAM surfaces described above are combined with a water box to characterize the water adsorption properties. For the *NVT* simulations, a fixed number of water molecules (325 molecules for the fluorinated SAM and 235 molecules for the other SAM systems) with vapor density 1.7×10^{-4} molecules/Å^3 were placed above the SAM. Ten different sets (labeled seed 1–10) of initial water coordinates were used for each SAM functional group (80 systems in total) in order to be able to assign error bars in the data analysis. Following Xu et al.,[19] the water vapor temperature was initialized at 450 K (which is the saturated vapor temperature for the considered initial vapor density of 5.08 kg/m^3), and the temperature of the SAM layer was maintained at 373 K.[19] The constant vapor density simulations were carried out by adding water vapor into the system to maintain a constant vapor density.

In all these simulations, a repulsive wall was placed at $z \approx$ 305 Å to prevent water molecules from diffusing across the periodic boundary onto the "back" side of the SAM. All the alkanethiol SAM molecules except the fully fluorinated ones were represented using the CHARMM general force field (CGenFF). The fully fluorinated alkanethiol parameters were obtained from Von Rudorff et al.[36] The fully flexible simple point charge/extended (SPC/E-F) water model[37] was selected because it has the correct liquid/vapor surface tension, which is crucial to accurately model condensation.

Simulation Details. All simulations were performed using the LAMMPS MDs software package. Periodic boundary conditions were applied in all three directions, and the Verlet algorithm was used to integrate the equations of motion with a time step of 0.5 fs. Lennard–Jones interactions were truncated at 10 Å, and long-range electrostatics were treated with the particle–particle particle–mesh solver with a real-space cutoff of 12 Å. Using a Langevin thermostat, the temperature of the SAM layer was kept constant at 373 K.

For the fixed number of water simulations, the velocities of the water molecules were initially sampled from the Maxwell–Boltzmann distribution at 450 K, and each simulation was run until more than 70% of the water condensed onto the surface. The time it takes for most (70%) of the water vapor to condense on the surface is measured and reported in Table 1 as the average of 10 simulations for each functional group. For the constant vapor density simulations, velocities of the added water were initialized at 450 K. When the water density in the vapor phase becomes less than 2×10^{-4} molecules/Å^3, new water was added to a specified region (150 Å < z < 270 Å) to maintain a constant vapor density. The LAMMPS input file used for the constant vapor density simulations is included in

https://dx.doi.org/10.1021/acs.langmuir.0c00915
Langmuir 2020, 36, 7383–7391

Table 1. Condensation Time and the Largest Cluster Size Reported for the Fixed Number of Water Simulations

SAM terminal group	average time taken for 70% of water in the system to condense on the surface (ps)	cluster size (number of water molecules) of the biggest cluster formed in the vapor phase
$-CF_3$	1973.0 ± 1113.8	240
$-CH_3$	1694.5 ± 932.5	151
$-OCH_3$	267.0 ± 41.2	19
$-CONHCH_3$	263.0 ± 48.2	15
$-CN$	145.0 ± 10.5	8
$-COOH$	136.0 ± 10.7	8
$-CONH_2$	130.0 ± 13.7	6
$-OH$	120.0 ± 5.3	6

the Supporting Information. All the simulation results were visualized using VMD.[38]

Details of Calculations. For the cluster analysis, all water oxygen atom coordinates were saved from the LAMMPS trajectory file using a Tcl script to represent the positions of water molecules. If the distance between two water molecules is less than 3.36 Å, they were considered to be part of the same cluster.[19] Then, for each cluster, the number of water molecules in the cluster and the smallest z-coordinate of the cluster were calculated. If the cluster size is greater than one molecule and the z-distance between the smallest z-value of the cluster and the SAM upper surface is also less than 3.36 Å, all the water molecules in the cluster were considered as deposited on the surface.

For the fixed number of water simulation trajectories, the normalized water count deposited on the surface (Figure S4) and in the vapor phase (Figure S5) was plotted against time to measure the cluster growth rate. Then, the rate of condensation was obtained from the average slopes, as shown in Figure S4, after the initiation of condensation and until 70% of the water is condensed.

For the density studies, time-averaged atom counts were recorded as a function of the z-coordinate during simulations at constant vapor density, which already had a thick water layer built up on the surface. For the energy analysis, we again used the constant vapor density trajectories after a thick condensed water layer has built up on the surface. We used overlapping histogram bins of width 0.5 Å in the z direction in order to measure the water−SAM energy as a function of the water slab z-position. Then, the total interaction energy between the dynamic water in those regions and the SAM molecules was computed with time. From the simulation data, the time-averaged total interaction energy density (E_D) used to plot Figure 6 was calculated by dividing by the volume of the selected region. To compute the energy contribution from the Lennard-Jones interactions, the trajectories were rerun (using the "rerun" command in LAMMPS) with an infinitely large dielectric constant (Figure S10). The heat transfer calculations, the hydrogen bond count analysis, and the solvent accessible surface area analysis are presented in detail in the Supporting Information.

RESULTS AND DISCUSSION

Rate of Condensation. We studied the condensation of water vapor on different cooled SAM surfaces: 1. with a fixed amount of water (initially all in the vapor phase) and 2. at constant water vapor density. Although this condensation process is nominally a heterogeneous nucleation process, on the molecular scale, we observed a wide range of behaviors from, at one extreme, a resemblance of homogeneous nucleation in the case of hydrophobic surfaces to, at the other extreme, film-wise condensation on hydrophilic surfaces. The time-lapse images of the simulation trajectories are shown in Figures 1, S2, and S3.

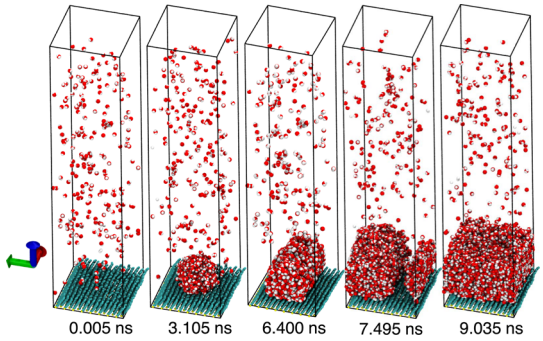

Figure 1. Snapshots of water condensation on the $-CH_3$-terminated SAM from a constant vapor density simulation. SAM chains are represented without hydrogens. The coloring is as follows: oxygen, red; hydrogen, white; and SAM chains, cyan.

In general, when a water molecule from the high-temperature vapor phase collides with the low-temperature surface, the (sensible heat) energy transfer results in a less energetic water molecule. In the case of a hydrophobic surface, this water molecule tends to return to the vapor phase where, through encounters with other water molecules, it can serve as a site for homogeneous nucleation (see Video S1 and Figure S2). Nucleation of water droplets in the vapor phase is counterproductive because the latent heat will not immediately be extracted by the surface. With a hydrophilic surface, homogeneous nucleation is suppressed because once a water molecule collides with the surface, its ability to return to the vapor phase is reduced because of its strong electrostatic interactions with surface atoms. Hence, the released latent heat from the resulting heterogeneous nucleation events can be readily extracted by the surface.[19,39−41]

In the current simulations, the initial vapor density is about 5.08 kg/m^3 (at 450 K), which is much higher than the saturated vapor density at 373 K of 0.598 kg/m^3,[42] and water molecules tend to condense toward equilibrium. Because SAM atoms are maintained at the condensation temperature (373 K) and no additional forces are applied to the water molecules, latent heat can only be exchanged at the SAM−water interface.[19,39] Therefore, during condensation, all the heat will be released to the surface/sink[39,41,43−49] (see Section S3 and Figures S12−S14 for more information).

A cluster analysis was performed to quantify the extent of heterogeneous and homogeneous nucleation as a function of the surface wettability (Figures 2 and 3). Clusters in the vapor phase can grow by capturing vapor-phase atoms or by coalescing with other clusters. Eventually, when a cluster is large enough, it can be captured by the surface upon collision (Figure S2). Figure 3 plots the ratio of the number of water molecules contained in vapor-phase clusters with size >1 to the total number of water molecules in the system, as a function of time for different SAM surfaces to show the extent of homogeneous nucleation. Over all the fixed number of water trials we performed, the largest cluster observed in the vapor phase comprised 151 water molecules for the $-CH_3$-

https://dx.doi.org/10.1021/acs.langmuir.0c00915
Langmuir 2020, 36, 7383−7391

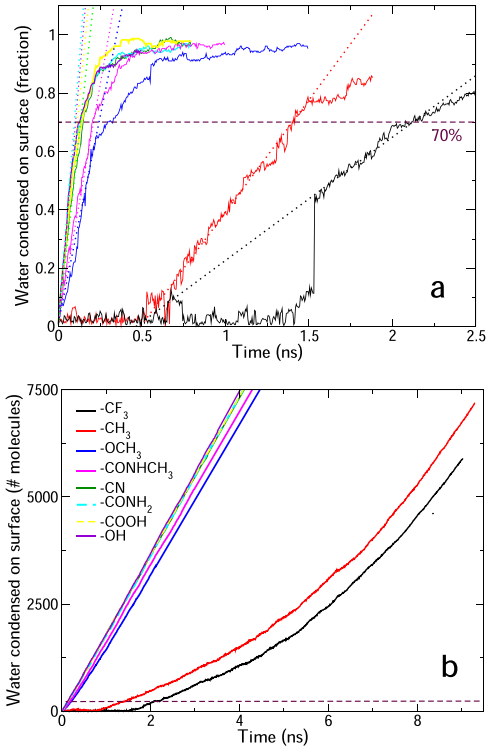

Figure 2. Summary of water condensed on the SAM surface. (a) Fixed number of water simulations: the ratio of the number of water molecules condensed on the surface to the total number of water molecules in the system versus time (seed 1 results only). (b) Constant vapor density simulations: the number of water molecules condensed on the surface versus time. The data are colored by the terminal SAM group. The maroon dotted line in both plots indicates the amount of water corresponding to 0.7 in panel a.

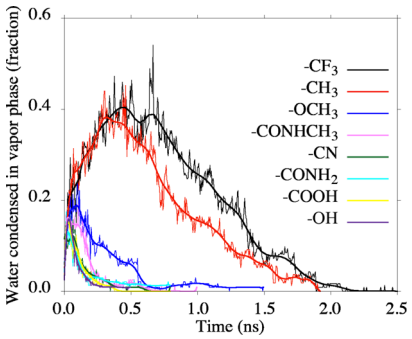

Figure 3. Ratio of the number of water molecules in vapor-phase clusters (size >1) to the total number of water molecules in the system versus time (seed 1 results from the fixed number of water trials). The data are colored by the terminal SAM group.

terminated SAM and 240 molecules for the fully fluorinated SAM. In all cases, we observe the formation of vapor-phase clusters (Figure 3), and the largest cluster size observed for each system is reported in Table 1. Small clusters are stabilized on hydrophilic surfaces by their hydrogen bonding interactions, whereas on hydrophobic surfaces, migrations along the surface and desorption of the droplets were observed in the MD trajectories (Figures S2 and S3).

As the SAMs become more hydrophilic, the droplet spreading and higher Kapitza conductance make the water-surface heat transfer more efficient (Section S3).[31] This transfer removes energy from the water molecules and hence tends to suppress desorption. Unlike in the hydrophobic cases, for hydrophilic surfaces, clusters become stable on the surface even at very small size because of their strong electrostatic interactions with the surface. Therefore, for the systems with more hydrophilic character, no large clusters are observed in the vapor phase, and the condensation rate is high (Table 1). Large clusters observed in the vapor phase and the low condensation rate show the strongly hydrophobic character of the $-CH_3$-terminated and fully fluorinated SAMs compared to the other cases. Therefore, the rates of condensation can be used to rank the wettability of different surfaces.

In Figure 2a, we observe that, once condensation initiates on the surface, the amount of water on the surface tends to increase linearly with time. However, for the hydrophobic surfaces, there is a time lag for condensation to initiate, which corresponds to the homogeneous nucleation regime. This time lag is highly variable, as seen in Figure S4, because it is governed by the dynamics of one or more large clusters, which infrequently encounter the surface. Moreover, in certain cases, the growth rate of water on the hydrophobic surfaces is not smooth with several sudden increases (Figure S4A,B), when sizeable clusters in the vapor phase adsorb onto the surface (or onto an existing droplet condensed on the surface, as shown in Figure S2). For the fixed number of water simulations, eventually all the water molecules condense on the surface. Therefore, the rate of condensation was obtained from the slopes of the curves (see Figures 2 and S4) after the initial time lag but before the linear growth rate tails off. Specifically, it is the slope from the initiation of condensation until roughly 70% of the water is condensed.

In the constant vapor density simulations, we see a very interesting behavior. For the hydrophilic surfaces, the amount of water condensed on the surface increases linearly with time (at a constant rate). However, for the hydrophobic surfaces, the rate of condensation increases with time (see Figure 2b).

The extent of wetting is determined by the balance of adhesive and cohesive forces acting on the condensed water droplets. On the most hydrophilic surfaces, water molecules tend to form a monolayer as soon as they condense. On lotus leaf-like superhydrophobic surfaces that contain some surface topography, water droplets tend to maintain a spherical shape.[50] However, on the flat hydrophobic surfaces considered here, the condensed water molecules tend to form hemispherical droplets. When the hydrophilic character of the surface increases, the clusters condensed on the surface will tend to change their shape from hemispherical to a monolayer (Figure S3). Under constant vapor density conditions, the monolayer thickness on the hydrophilic surfaces tends to increase at a constant rate (Figure 2b). For the hydrophobic cases, hemispherical water droplets will initially form on the surface. Therefore, similar to the fixed amount of water simulations, the condensation results of the constant vapor density simulations in Figure 2b show slower rates of condensation for both $-CH_3$-terminated and fully fluorinated surfaces until the droplets on the surface coalesce to form hemicylinders and eventually form a thick uniform film of water (Figure 1).

As more and more water condenses making a thick film of water, the water in the vapor phase effectively sees a hydrophilic surface (of water), which results in a high condensation rate. Because of this, ~7.5 ns later, the condensation rate of the hydrophobic systems becomes roughly equal to that of the hydrophilic surfaces (Figure 2b).

https://dx.doi.org/10.1021/acs.langmuir.0c00915
Langmuir 2020, 36, 7383−7391

For all the systems, after some time, water vapor condenses onto an existing liquid water layer, but there are still small differences in the deposition rates because of the efficiency of heat transfer as characterized by the Kapitza conductance.

Thus, according to the rates of condensation, the order of surface wettability can be characterized as $-OH > -CONH_2 > -COOH > -CN > -CONHCH_3 \approx -OCH_3 > -CH_3 > -CF_3$. The OH terminal group can orient (Figure S11b) easily in water to capture approaching water molecules. Hence, the −OH-terminated SAM shows the highest rate of condensation. The next highest rates of condensation of $-CONH_2$, −COOH, and −CN follow the order of their polarity ranking. Even though amides have higher polarity because of the oxygen and nitrogen atoms in them, the methyl group adds some nonpolar character and reduces the hydrophilicity of the $-CONHCH_3$-terminated SAM. Similarly, the $-CH_3$ terminus makes the ether more hydrophobic, but the presence of the oxygen atom will allow it to participate in hydrogen bonding with water molecules. The fully fluorinated SAM shows the lowest rate of condensation among all the systems. This is consistent with its enhanced hydrophobicity, which arises because the fluorocarbon SAM chains pack less densely than their hydrocarbon counterparts (30.1 Å^2 per chain vs 21.6 Å^2), resulting in weaker van der Waals interactions with water.[35]

Experimental contact angle measurements are made on micro or millimeter size droplets. Although line tension effects can alter the contact angle of nanoscale droplets,[52] Xu et al.[19] and Shenogina et al.[31] reported that the nanoscale droplets observed by MD simulation seem to have wettability and contact angles consistent with their macroscopic counterparts. Hence, to compare data across different studies, we decided to use the experimental contact angles to quantify surface wettability.

To demonstrate consistency with previous results, we compare our condensation rate data with that of Xu[19] in Figure S7. Although the surfaces used in Xu et al.[19] are of a very different nature than ours, the results are in excellent agreement except for the very hydrophilic surfaces, which essentially all have the same contact angle.

In a series of landmark papers, Garde and co-workers developed a microscopic measure of surface wettability based on the compressibility of water. The general idea is that a hydrophobic surface tends to promote water depletion near the surface and induce formation of a liquid/vapor-like interface while water near a hydrophilic surface is in a tight solvation environment because of strong hydrogen bonding interactions with the surface (see Figure S6). Therefore, the compressibility of water near a hydrophobic surface is higher than that near a hydrophilic surface. In Figure 4a, we plot the compressibility ratio metric from Acharya et al.,[34] and our condensation results against the contact angle. The correlation is remarkable. The data indicate a reciprocal relationship between the compressibility and the rate of condensation. We can see when the hydrophilicity of a surface increases, the condensation rate increases, and the condensed water forms a stable film because of a network of hydrogen bonds reducing the compressibility. However, in the hydrophobic case, the formation of a vapor-like water depletion layer (Figure S6) at the interface will cause an increase in the compressibility of the interfacial water.

Because there is a vapor-like layer of water near a hydrophobic surface, one would expect poor thermal conductance across the solid−liquid interface, which would inhibit condensation because the latent heat cannot be

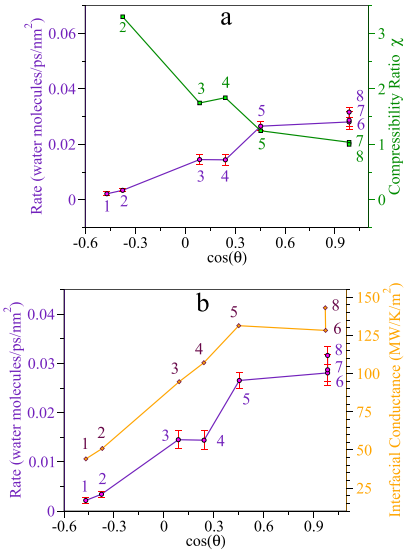

Figure 4. (a) Rate of condensation (number of water molecules/ps/nm^2) obtained from the fixed number of water simulations and the compressibility ratio χ extracted from Acharya et al.[34] using the g3data[51] extraction tool, plotted against the contact angle. (b) Rate of condensation obtained for the fixed number of water simulations and the interfacial thermal conductance extracted from Shenogina et al.[31] using g3data, plotted against the contact angle. Data points labeled: fully fluorinated SAM (1), $-CH_3$- (2), $-OCH_3$- (3), $-CONHCH_3$- (4), −CN- (5), −COOH- (6), $-CONH_2$- (7), and −OH- (8)terminated SAMs.

efficiently removed (Figure S12). On the other hand, hydrogen bonding between water molecules and hydrophilic surface functional groups gives a direct vibrational coupling, which increases the thermal conductance. Indeed, Shenogina et al.[31] showed that the Kapitza conductance is proportional to the work of adhesion, $G_k \propto W = \gamma_{AW}(1 + \cos\theta)$, where γ_{AW} is the air−water surface tension, which correlates very well with our condensation data, as plotted in Figure 4b.

Density Analysis. In order to provide molecular insight into the condensation rates and to understand the behavior of water near the interface as a function of surface chemistry, density profiles normal to the SAM−water interface were constructed for the eight different SAMs using a thick layer of water deposited from the constant vapor density simulations (Figure 5). The water density profiles in all cases display an interfacial region of varying density and a bulk region of constant density (Figures 5 and S8). In the interfacial region, a layering[53] of water arises from the planar surface. The superimposed water profiles in Figure S8 clearly show comparatively lower z locations of the first peak for hydrophilic SAMs, and a more pronounced second structured layer of water in surfaces that have some hydrophobic character. Water density profiles observed near the SAM surface show similar spatial oscillations to the profiles reported by Jamadagni et al.[32] As mentioned by Godawat et al.,[33] we saw no correlation between the height of the first peak and the surface wettability.

The overlap of the water profile with the SAM profile quantifies the extent of water penetration into the surface (Table S1). The hydrophobic systems, namely the $-CH_3$-terminated SAM and the fully fluorinated SAM, show a depletion layer with essentially zero overlap, which has been observed in previous experimental and simulation studies.[28,54,55] The presence of a depletion layer is consistent

https://dx.doi.org/10.1021/acs.langmuir.0c00915
Langmuir 2020, 36, 7383−7391

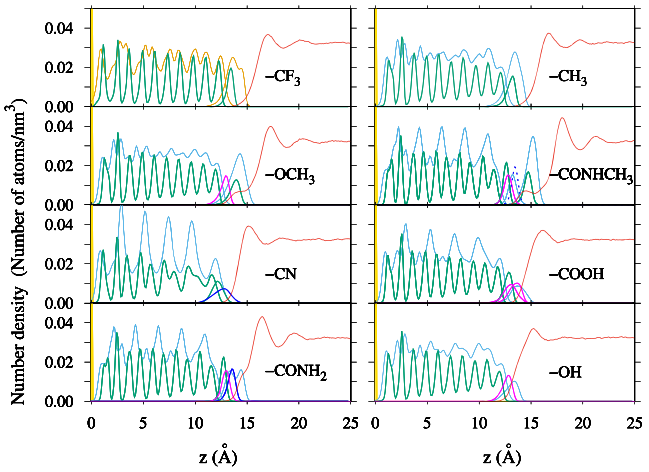

Figure 5. Water and SAM atom density profiles along z for fully fluorinated, $-CH_3$-, $-OCH_3$-, $-CONHCH_3$-, $-CN$-, $-COOH$-, $-CONH_2$-, and $-OH$-terminated SAM systems. Coloring is as follows: sulfur, yellow; carbon, green; nitrogen, blue; oxygen, magenta; hydrogen, light-blue; fluorine, orange; and water, red.

with low thermal conductance and high compressibility as previously discussed.

For all the other systems, we observed overlapping density profiles between water and SAM. These overlapping density profiles indicate water penetration into the SAM to form hydrogen bonds with oxygen- and nitrogen-containing functional groups (see Figure S9a for the hydrogen bond analysis). For the $-OH$-, $-CONH_2$-, $-COOH$-, and $-CN$-terminated SAMs, where the hydrogen bonding group is at the chain end, the rate of condensation and the area overlap of the density profiles are in the same order. For the $-OCH_3$- and $-CONHCH_3$-terminated SAMs, the hydrogen bonding groups are covered by a $-CH_3$ terminal group, so that water molecules need to penetrate deeper to find more electronegative atoms. Hence, the largest overlap (Table S1) of water in the density profile will not always reveal the most hydrophilic surface.

The order is little bit different if we categorize the systems according to the average hydrogen bond count between water and SAM functional groups, as plotted in Figure S9a, $-OH > -COOH > -CONH_2 > -CONHCH_3 > -OCH_3 > -CN \gg -CF_3 > -CH_3$. This is mainly because when a water molecule penetrates into the SAM layer to make hydrogen bonds with SAM atoms, it can bring with it other water molecules that are already hydrogen bonded to each other. This means not all the water that is penetrated into the SAM will make hydrogen bonds with SAM atoms. Therefore, even though we see the largest overlap in the density profiles for the $-CONHCH_3$- and $-OCH_3$-terminated SAM systems, the number of hydrogen bonds they make with water is lower than that of the $-OH$-, $-COOH$-, and $-CONH_2$-terminated SAMs.

The average hydrogen bond count of the $-CN$-terminated SAM observed in Figure S9a is greater than that of fully fluorinated SAM but lower than the $-CONHCH_3$-terminated SAM and the $-OCH_3$-terminated SAM. However, we observed higher rates of water condensation for the $-CN$-terminated SAM compared to the above three systems ($-CONHCH_3$, $-OCH_3$, and fully fluorinated SAM). Water hydrogen atoms can readily form hydrogen bonds with the nitrile group because the nitrile group is at the terminus of the SAM chain and is therefore more exposed to water than the buried electronegative atoms in the $-CONHCH_3$ and $-OCH_3$ SAMs. In addition, the linearity of the nitrile group can alleviate possible steric issues. However, in theory, we would expect more hydrogen bonding between water and SAM atoms in the $-CONHCH_3$ and $-OCH_3$ systems compared to the $-CN$-terminated SAM because the $-CONHCH_3$ group has a hydrogen atom bonded to a nitrogen and two pairs of nonbonded electrons on the oxygen, and the $-OCH_3$ group has two nonbonding electron pairs, allowing multiple possible sites for hydrogen bonding with water. Although for the $-CN$ group, only one lone pair of electrons is available on the nitrogen atom to act as a site to form hydrogen bonds with water. Hence, even though the $-CN$-terminated SAM shows a lower hydrogen bond count compared to the $-CONHCH_3$- and the $-OCH_3$-terminated SAMs, the molecular geometry and the partial charges on the atoms account for the higher condensation rate.

Collectively, these data show that the water behavior near the surface is very sensitive to surface chemistry. The amount of water penetrated inside the SAM will not always reveal the interaction strength between water and SAM, but the hydrogen bond count can explain the stabilization of water once it is condensed on the surface.

Interaction Energy Analysis. As a more direct approach to characterize surface wettability, we measured the interaction energy between the SAM and water. The time-averaged electrostatic, van der Waals, and total interaction energy between the water and the SAM were calculated in slices along the direction (z) normal to the SAM surface. Then, the interaction energy density distribution (interaction energy/volume of a slice) along the z direction is plotted in Figures 6

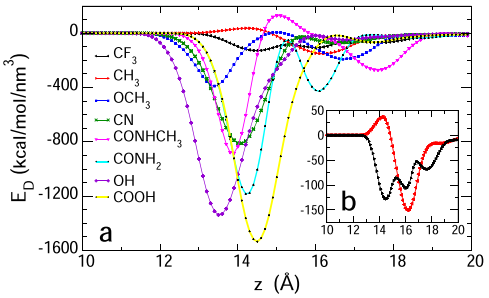

Figure 6. (a) Time-averaged total interaction energy density (E_D) with respect to the z distance between water and the fully fluorinated, $-CH_3$-, $-OCH_3$-, $-CONHCH_3$-, $-CN$-, $-CONH_2$-, $-OH$-, and $-COOH$-terminated SAMs. (b). Inset shows the interaction energy densities of the fully fluorinated (black) and $-CH_3$-terminated (red) systems. Here, the interaction energy density is defined as the ratio of the interaction energy to the volume of a slice.

and S10. The SAM hydrocarbon chains exclude water until z = 11.5 Å, as shown in Figure 6. For different systems, the SAM–water interface is located at different z values because of the size and wettability of the SAM head group. Therefore, the place where the interaction energy first becomes nonzero will be different for the different SAM systems. In general, we see one or more energy minima representing favorable interactions between water and the SAM, which contributes to the condensation process.

The three methyl-terminated SAMs ($-CH_3$, $-O-CH_3$, and $-CONH-CH_3$) are the only systems, in which the overall interaction energy is repulsive ($E_D > 0$) at some z-value (see Figure S10). Typically, water molecules orient near a

https://dx.doi.org/10.1021/acs.langmuir.0c00915
Langmuir 2020, 36, 7383−7391

hydrophobic surface to maximum hydrogen bonding with other water molecules, and this puts the water near the surface in an orientation (Figure S11b) that can make the SAM−water electrostatic energy unfavorable. This electrostatic repulsion in the case of the $-CH_3$-terminated SAM coincides with the depletion zone observed in the density analysis. Even though the fully fluorinated SAM showed the most hydrophobic characteristics in the previous analyses, unlike the $-CH_3$-terminated SAM, an initial decrease in total energy was observed because of fluorine's hydrogen bond-forming ability. However, when we compare the $-CH_3$-terminated SAM and the fully fluorinated SAM in Figure 6b, the fully fluorinated SAM still gives the shallowest minimum interaction energy, −128 kcal/mol/nm^3 (Table 2), verifying its previously observed most hydrophobic character. The total interaction energy of −COOH-, −OH-, and $-CONH_2$-terminated SAMs is mainly attributed to the electrostatic attraction between the SAM and water. Interestingly, for the −COOH and −OH SAM systems, the very large (favorable) electrostatic interaction pulls the atoms together into the repulsive van der Waals regime (Figure S10).

Table 2. Minimum Interaction Energy with the z Distance

SAM terminal	minimum energy density/(kcal/mol/nm^3)	z distance/Å
$-CF_3$	−128	14.5
$-CH_3$	−151	16.2
$-OCH_3$	−389	13.4
$-CONHCH_3$	−883	13.8
−CN	−811	14.1
$-CONH_2$	−1183	14.2
−OH	−1338	13.5
−COOH	−1535	14.5

A deeper minimum indicates stronger interactions between the SAM and water, which can drive the water condensation process. Therefore, according to the interaction energy minima of Figure 6 recorded in Table 2, we can rank the water−SAM interactions as follows: −COOH > −OH > $-CONH_2$ > $-CONHCH_3$ > −CN > $-OCH_3$ > $-CH_3$ > $-CF_3$. This result agrees well with our condensation rate results except that we see the highest interaction energy between the water and the −COOH-terminated SAM instead of the −OH terminated-SAM. In general, carboxylic acids can form more hydrogen bonds than alcoholic functional groups because they can serve as both a hydrogen-bond donor and an acceptor, and their OH group is more strongly polarized than the alcoholic OH group. However, in Figure S9b, we see that the −COOH-functionalized SAM forms fewer intermolecular hydrogen bonds with water than the −OH-terminated SAM because it uses most of its available sites to form intermolecular hydrogen bonds with the other neighboring SAM molecules. Thus, we can rationalize the lower rate of water condensation for the −COOH-terminated SAM compared to the −OH-terminated SAM. As explained in the density analysis, we observed a lower interaction energy for the −CN-terminated SAM compared to the $-CONHCH_3$-terminated SAM, even though we observed a higher rate of condensation for the former. Hence, we see that for water condensation, we need to consider not only the interaction energy between water and the SAM but also the functional group geometry, accessibility, partial charges, steric effects, and the ability to form hydrogen bonds for stabilization on the surface.

CONCLUSIONS

In summary, we have performed MD computer simulations to quantify the role of surface wettability in water condensation using well characterized SAM surfaces of alkanethiols with different head group chemistries. The rate of water condensation on different cooled SAM surfaces was studied using two different models: 1. with a fixed amount of water (initially all in the vapor phase) and 2. with a constant vapor density. The measured water condensation rates were linked to other properties dependent on surface wettability such as the water contact angle, compressibility, and interfacial thermal conductance to give a more complete picture of the role of surface wettability on water condensation. During the simulations, the formation and growth mechanism of clusters and the wetting process of the surface were investigated. The water density near the surface was studied to quantify the water penetration into the SAM. From a hydrogen bond count analysis, we provided insight into the condensation rate results and explained the stability and the structural arrangements of water as a function of the surface chemistry. We correlated the rate of condensation to the interaction energy between water molecules and the SAM.

We noticed at hydrophobic surfaces, because of the observed weak interaction energies, water molecules or small water clusters that encounter the surface tend to escape into the vapor phase, serving as potential homogeneous nucleation sites. Hence, sizeable clusters were observed in the vapor phase. However, when the cluster is large enough, it was captured by the surface upon collision and assumed the shape of a hemisphere.

For hydrophilic surfaces, strong interaction energies were observed between water molecules and SAM functional groups. This restricts the formation of vapor-phase clusters, and thus, mainly heterogeneous nucleation was observed. A greater wettability was observed with increasing surface hydrophilicity which gives rise to a higher Kapitza conductance. Therefore, higher condensation rates were observed for hydrophilic SAMs. The surface wettability was characterized by SAM head group chemistry according to the condensation rates as −OH > $-CONH_2$ > −COOH > −CN > $-CONHCH_3 \approx -OCH_3$ > $-CH_3$ > $-CF_3$.

Observed repulsive interaction energy regions and the nonoverlapping water density profiles with SAM atoms indicate a liquid/vapor-like interface caused by water depletion at hydrophobic interfaces. This water depletion layer and the lower hydrogen bond count (no direct vibrational coupling) reduce the thermal conductance across the solid−liquid interface, which inhibits the condensation because the latent heat cannot be efficiently removed by the substrate. At the same time, the depletion layer results in a high compressibility of the interfacial water as observed by Acharya et al.[34]

Taking all the results of this investigation into account, we were able to give a more complete molecular-level picture of the water condensation process on surfaces of different wettabilities and provide connections with other microscopic and macroscopic interfacial characterizations. The provided microscopic insight into the water behavior as a function of surface wettability can be used to improve the design of substrates for water condensation.

https://dx.doi.org/10.1021/acs.langmuir.0c00915
Langmuir 2020, 36, 7383−7391

■ ASSOCIATED CONTENT

Supporting Information

The Supporting Information is available free of charge at https://pubs.acs.org/doi/10.1021/acs.langmuir.0c00915.

The hydrogen bond count analysis, the solvent accessible surface area analysis, the heat transfer and temperature calculation, supplementary Figures S1−S14, and supplementary Table S1 and the legend of the video (PDF)

Video S1 (MP4)

■ AUTHOR INFORMATION

Corresponding Author

Steven O. Nielsen − *Department of Chemistry and Biochemistry, The University of Texas at Dallas, Richardson, Texas 75080, United States;* orcid.org/0000-0003-3390-3313; Email: steven.nielsen@utdallas.edu

Authors

Dineli T. S. Ranathunga − *Department of Chemistry and Biochemistry, The University of Texas at Dallas, Richardson, Texas 75080, United States;* orcid.org/0000-0002-7860-722X

Alexandra Shamir − *Department of Chemistry and Biochemistry, The University of Texas at Dallas, Richardson, Texas 75080, United States;* orcid.org/0000-0002-6363-4655

Xianming Dai − *Department of Mechanical Engineering, The University of Texas at Dallas, Richardson, Texas 75080, United States;* orcid.org/0000-0001-5050-2867

Complete contact information is available at: https://pubs.acs.org/10.1021/acs.langmuir.0c00915

Notes

The authors declare no competing financial interest.

■ ACKNOWLEDGMENTS

X.D. acknowledges the National Science Foundation (award no. 1929677) and the Young Investigator Program at Army Research Office (award no. W911NF1910416).

■ REFERENCES

(1) Dai, X.; Sun, N.; Nielsen, S. O.; Stogin, B. B.; Wang, J.; Yang, S.; Wong, T. S. Hydrophilic directional slippery rough surfaces for water harvesting. *Sci. Adv.* **2018**, *4*, No. eaaq0919.

(2) Desert, N.; Desert, T. N. Water capture by a desert beetle. *Nature* **2001**, *414*, 33−34.

(3) Lee, A.; Moon, M.-W.; Lim, H.; Kim, W.-D.; Kim, H.-Y. Water harvest via dewing. *Langmuir* **2012**, *28*, 10183−10191.

(4) Rykaczewski, K.; Scott, J. H. J.; Rajauria, S.; Chinn, J.; Chinn, A. M.; Jones, W. Three dimensional aspects of droplet coalescence during dropwise condensation on superhydrophobic surfaces. *Soft Matter* **2011**, *7*, 8749−8752.

(5) Khawaji, A. D.; Kutubkhanah, I. K.; Wie, J.-M. Advances in seawater desalination technologies. *Desalination* **2008**, *221*, 47−69.

(6) Humplik, T.; Lee, J.; O'Hern, S. C.; Fellman, B. A.; Baig, M. A.; Hassan, S. F.; Atieh, M. A.; Rahman, F.; Laoui, T.; Karnik, R.; Wang, E. N. Nanostructured materials for water desalination. *Nanotechnology* **2011**, *22*, 292001.

(7) Xiao, R.; Miljkovic, N.; Enright, R.; Wang, E. N. Immersion Condensation on Oil-Infused Heterogeneous Surfaces for Enhanced Heat Transfer. *Sci. Rep.* **2013**, *3*, 1988.

(8) Daniel, S.; Chaudhury, M. K.; Chen, J. C. Linked references are available on JSTOR for this article : Fast Drop Movements Resulting from the Phase Change on a Gradient Surface. **2016**, *291*, 633−636.

(9) Anand, S.; Paxson, A. T.; Dhiman, R.; Smith, J. D.; Varanasi, K. K. Enhanced condensation on lubricant-impregnated nanotextured surfaces. *ACS Nano* **2012**, *6*, 10122−10129.

(10) Alizadeh, A.; Bahadur, V.; Kulkarni, A.; Yamada, M.; Ruud, J. A. Hydrophobic surfaces for control and enhancement of water phase transitions. *MRS Bull.* **2013**, *38*, 407−411.

(11) Miljkovic, N.; Enright, R.; Nam, Y.; Lopez, K.; Dou, N.; Sack, J.; Wang, E. N. Jumping-droplet-enhanced condensation on scalable superhydrophobic nanostructured surfaces. *Nano Lett.* **2013**, *13*, 179−187.

(12) Su, B.; Tian, Y.; Jiang, L. Bioinspired Interfaces with Superwettability: From Materials to Chemistry. *J. Am. Chem. Soc.* **2016**, *138*, 1727−1748.

(13) Pinheiro, R. A.; Silva, A. A.; Trava-Airoldi, V. J.; Corat, E. J. Water vapor condensation and collection by super-hydrophilic and super-hydrophobic VACNTs. *Diamond Relat. Mater.* **2018**, *87*, 43−49.

(14) Zhai, L.; Berg, M. C.; Cebeci, F. Ç.; Kim, Y.; Milwid, J. M.; Rubner, M. F.; Cohen, R. E. Patterned superhydrophobic surfaces: Toward a synthetic mimic of the namib desert beetle. *Nano Lett.* **2006**, *6*, 1213−1217.

(15) Bai, H.; Wang, L.; Ju, J.; Sun, R.; Zheng, Y.; Jiang, L. Efficient water collection on integrative bioinspired surfaces with star-shaped wettability patterns. *Adv. Mater.* **2014**, *26*, 5025−5030.

(16) Hou, Y.; Yu, M.; Chen, X.; Wang, Z.; Yao, S. Recurrent filmwise and dropwise condensation on a beetle mimetic surface. *ACS Nano* **2015**, *9*, 71−81.

(17) Wong, T.-S.; Kang, S. H.; Tang, S. K. Y.; Smythe, E. J.; Hatton, B. D.; Grinthal, A.; Aizenberg, J. Bioinspired self-repairing slippery surfaces with pressure-stable omniphobicity. *Nature* **2011**, *477*, 443−447.

(18) Park, K.-C.; Kim, P.; Grinthal, A.; He, N.; Fox, D.; Weaver, J. C.; Aizenberg, J. Condensation on slippery asymmetric bumps. *Nature* **2016**, *531*, 78−82.

(19) Xu, W.; Lan, Z.; Peng, B. L.; Wen, R. F.; Ma, X. H. Effect of surface free energies on the heterogeneous nucleation of water droplet: A molecular dynamics simulation approach. *J. Chem. Phys.* **2015**, *142*, 054701.

(20) Xu, W.; Lan, Z.; Peng, B. L.; Wen, R. F.; Ma, X. H. Effect of nano structures on the nucleus wetting modes during water vapour condensation: From individual groove to nano-array surface. *RSC Adv.* **2016**, *6*, 7923−7932.

(21) Szöri, M.; Tobias, D. J.; Roeselová, M. Microscopic wetting of mixed self-assembled monolayers: a molecular dynamics study. *J. Phys. Chem. B* **2009**, *113*, 4161−4169.

(22) Szőri, M.; Jedlovszky, P.; Roeselová, M. Water adsorption on hydrophilic and hydrophobic self-assembled monolayers as proxies for atmospheric surfaces. A grand canonical Monte Carlo simulation study. *Phys. Chem. Chem. Phys.* **2010**, *12*, 4604.

(23) Szoöri, M.; Roeselová, M.; Jedlovszky, P. Surface hydrophilicity-dependent water adsorption on mixed self-assembled monolayers of C7-CH3 and C7-COOH residues. A grand canonical monte carlo simulation study. *J. Phys. Chem. C* **2011**, *115*, 19165−19177.

(24) Sheng, Q.; Sun, J.; Wang, Q.; Wang, W.; Wang, H. S. On the onset of surface condensation: Formation and transition mechanisms of condensation mode. *Sci. Rep.* **2016**, *6*, 1−9.

(25) Sheng, Q.; Sun, J.; Wang, W.; Wang, H. S.; Bailey, C. G. How solid surface free energy determines coalescence-induced nanodroplet jumping: A molecular dynamics investigation. *J. Appl. Phys.* **2017**, *122*, 245301.

(26) Niu, D.; Tang, G. H. The effect of surface wettability on water vapor condensation in nanoscale. *Sci. Rep.* **2016**, *6*, 1−6.

(27) Niu, D.; Guo, L.; Hu, H. W.; Tang, G. H. Dropwise condensation heat transfer model considering the liquid-solid

interfacial thermal resistance. *Int. J. Heat Mass Transfer* **2017**, *112*, 333−342.
(28) Maccarini, M. Water at solid surfaces: A review of selected theoretical aspects and experiments on the subject. *Biointerphases* **2007**, *2*, MR1−MR15.
(29) Sun, J.; Wang, H. S. On the early and developed stages of surface condensation: Competition mechanism between interfacial and condensate bulk thermal resistances. *Sci. Rep.* **2016**, *6*, 1−12.
(30) Hiratsuka; Emoto; Konno; Ito. Molecular Dynamics Simulation of the Influence of Nanoscale Structure on Water Wetting and Condensation. *Micromachines* **2019**, *10*, 587.
(31) Shenogina, N.; Godawat, R.; Keblinski, P.; Garde, S. How wetting and adhesion affect thermal conductance of a range of hydrophobic to hydrophilic aqueous interfaces. *Phys. Rev. Lett.* **2009**, *102*, 1−4.
(32) Jamadagni, S. N.; Godawat, R.; Garde, S. Hydrophobicity of Proteins and Interfaces: Insights from Density Fluctuations. *Annu. Rev. Chem. Biomol. Eng.* **2011**, *2*, 147−171.
(33) Godawat, R.; Jamadagni, S. N.; Garde, S. Characterizing hydrophobicity of interfaces by using cavity formation, solute binding, and water correlations. *Proc. Natl. Acad. Sci. U.S.A.* **2009**, *106*, 15119−15124.
(34) Acharya, H.; Vembanur, S.; Jamadagni, S. N.; Garde, S. Mapping hydrophobicity at the nanoscale : Applications to heterogeneous surfaces and proteins. **2010**, *146*, 353−365. DOI: 10.1039/b927019a
(35) Dalvi, V. H.; Rossky, P. J. Molecular origins of fluorocarbon hydrophobicity. *Proc. Natl. Acad. Sci. U.S.A.* **2010**, *107*, 13603−13607.
(36) Von Rudorff, G. F.; Watermann, T.; Sebastiani, D. Perfluoroalkane force field for lipid membrane environments. *J. Phys. Chem. B* **2014**, *118*, 12531−12540.
(37) López-Lemus, J.; Chapela, G. A.; Alejandre, J. Effect of flexibility on surface tension and coexisting densities of water. *J. Chem. Phys.* **2008**, *128*, 174703.
(38) Humphrey, W.; Dalke, A.; Schulten, K. VMD: Visual molecular dynamics. *J. Mol. Graph.* **1996**, *14*, 33−38.
(39) Hu, H.; Li, Q.; Liu, S.; Fang, T. Molecular dynamics study on water vapor condensation and infiltration characteristics in nanopores with tunable wettability. *Appl. Surf. Sci.* **2019**, *494*, 249−258.
(40) Mao, Y.; Zhang, Y. Molecular dynamics simulation on rapid boiling of water on a hot copper plate. *Appl. Therm. Eng.* **2014**, *62*, 607−612.
(41) Wang, S.; Wang, C.; Peng, Z.; Chen, S. Spontaneous dewetting transition of nanodroplets on nanopillared surface. *Nanotechnology* **2020**, *31*, 225502.
(42) Saturated Vapor Pressure, Density for Water in Hyperphysics Website. 2000, http://hyperphysics.phy-astr.gsu.edu/hbase/Kinetic/watvap.html#c1 (accessed 5/16/2020).
(43) Liang, Z.; Biben, T.; Keblinski, P. Molecular simulation of steady-state evaporation and condensation: Validity of the Schrage relationships. *Int. J. Heat Mass Transfer* **2017**, *114*, 105−114.
(44) Li, J.; Gao, S.; Long, R.; Liu, W.; Liu, Z. Self-pumped evaporation for ultra-fast water desalination and power generation. *Nano Energy* **2019**, *65*, 104059.
(45) Cha, H.; Vahabi, H.; Wu, A.; Chavan, S.; Kim, M.-K.; Sett, S.; Bosch, S. A.; Wang, W.; Kota, A. K.; Miljkovic, N. Dropwise condensation on solid hydrophilic surfaces. *Sci. Adv.* **2020**, *6*, No. eaax0746.
(46) Chilukoti, H. K.; Zhou, T.; Ardham, V. R.; Böhm, M. C.; Müller-Plathe, F. Thermal Energy Transport across the Interface between Phase Change Material n-Heneicosane in Solid and Liquid Phases and Few-Layer Graphene. *J. Phys. Chem. C* **2019**, *123*, 29192−29202.
(47) Cao, A. Molecular dynamics simulation study on heat transport in monolayer graphene sheet with various geometries. *J. Appl. Phys.* **2012**, *111*, 083528.
(48) Cao, Q.; Cui, Z. Molecular dynamics simulations of the effect of surface wettability on nanoscale liquid film phase-change. *Numer. Heat Transfer, Part A* **2019**, *75*, 533−547.
(49) Diaz, R.; Guo, Z. A molecular dynamics study of phobic/philic nano-patterning on pool boiling heat transfer. *Heat Mass Tran.* **2017**, *53*, 1061−1071.
(50) Courbin, L. Rethinking Superhydrophobicity. *Physics* **2016**, *9*, 9−10.
(51) Casey, J. g3data Website. https://directory.fsf.org/wiki/G3data (accessed 12/2/2019).
(52) Murai, J.; Marukawa, T.; Mima, T.; Arai, S.; Sasaki, K.; Saka, H. Size dependence of the contact angle of liquid clusters of Bi and Sn supported on SiO2, Al2O3, graphite, diamond and AlN. *J. Mater. Sci.* **2006**, *41*, 2723−2727.
(53) Ingebrigtsen, T.; Toxvaerd, S. Contact angles of Lennard-Jones liquids and droplets on planar surfaces. *J. Phys. Chem. C* **2007**, *111*, 8518−8523.
(54) De Gennaro Colonna, V.; Rossoni, G.; Bernareggi, M.; Müller, E. E.; Berti, F. Hexarelin, a growth hormone-releasing peptide, discloses protectant activity against cardiovascular damage in rats with isolated growth hormone deficiency. *Cardiologia* **1997**, *42*, 1165−1172.
(55) Janeček, J.; Netz, R. R. Interfacial water at hydrophobic and hydrophilic surfaces: Depletion versus adsorption. *Langmuir* **2007**, *23*, 8417−8429.

https://dx.doi.org/10.1021/acs.langmuir.0c00915
Langmuir 2020, 36, 7383−7391